Journal of Alloys and Compounds 509 (2011) 691–696

Contents lists available at ScienceDirect

Journal of Alloys and Compounds

journal homepage: www.elsevier.com/locate/jallcom

Biocompatibility of metal carbides on Fe–Al–Mn-based alloys

Chau-Hsiang Wang[a,b], Chin-Wan Luo[c,d,e,1], Chiung-Fang Huang[c,d,f], Mao-Suan Huang[c,d,e,**], Keng-Liang Ou[c,g,h,*], Chih-Hua Yu[c,g,i]

[a] School of Dentistry, College of Dental Medicine, Kaohsiung Medical University, Kaohsiung 807, Taiwan
[b] Department of Dentistry, Kaohsiung Medical University Hospital, Kaohsiung 807, Taiwan
[c] Research Center for Biomedical Devices, Taipei Medical University, Taipei 110, Taiwan
[d] School of Dentistry, College of Oral Medicine, Taipei Medical University, Taipei 110, Taiwan
[e] Department of Dentistry, Taipei Medical University-Shuang Ho Hospital, Taipei 235, Taiwan
[f] Department of Dentistry, Taipei Medical University Hospital, Taipei 110, Taiwan
[g] Research Center for Biomedical Implants and Microsurgery Devices, Taipei Medical University, Taipei 110, Taiwan
[h] Graduate Institute of Biomedical Materials and Engineering, Taipei Medical University, Taipei 110, Taiwan
[i] Biomate Medical Devices Technology Co. Ltd., Kaohsiung 806, Taiwan

ARTICLE INFO

Article history:
Received 8 October 2009
Received in revised form 8 June 2010
Accepted 11 June 2010
Available online 23 June 2010

Keywords:
Fe–Al–Mn-based alloy
Phase transformations
Surface functionalization
Biocompatibility

ABSTRACT

The biocompatibility and microstructural variation of Fe–Al–Mn (FAM)-based alloys have been investigated clearly. The ($(Fe,Mn)_3AlC_x$) carbide (κ′-carbide) and $Fe_{0.6}Mn_{5.4}C_2$ carbide (κ-carbide) as well as Cr_7C_3 (Cr-carbide) were formed on FAM alloy, following phase transformation by heat treatment and surface functionalization. These carbides have important role in forming nanostructure and oxidation layer. Moreover, it was found that the albumin adsorbed onto the surface increased with increasing nano-metal carbides. Therefore, heat treatment and surface functionalization such as electro-discharging and anodization not only generates a nanostructural precipitates, but also converts the alloy surface into a nanostructured oxide surface, then increasing the alloy biocompatibility.

1. Introduction

Metallic biomaterials such as cobalt-based alloys, ferrous-based alloys and titanium-based alloys exhibit superior characteristics for biomedical applications due to their high specific strength, and biocompatibility [1–10]. All of them are used as metallic structural biomaterials such as artificial hip joints and dental implants for application in replacement of hard tissue. Ferrous-based alloys such as stainless steel are widely applied in coronary stents and temporary implants [11–14]. However, the exposure to flowing blood of the ferrous-based alloys that are employed can lead to thrombus formation and smooth muscle cell proliferation, and ultimately result in restenosis and poor initial hemocompatibility for temporary implants. To avoid these effects, a great amount of researches have attempted to develop nonthrombogenic coatings for these ferrous-based alloys [15,16]. Albumin has been found to be passive to both bacteria and platelets. A confluent layer of albumin can be both anti-infective and anti-thrombogentic [17]. Several techniques have been employed for the preparation of surfaces covered with albumin, including covalent binding of albumin, covalent binding of an albumin trigger ligand and simple methods of absorbing albumin directly on the substrate surface [18–21]. However, most of these methods require special treatments on substrate topography.

The current research explores a new procedure for generating nanostructural surfaces and nano-precipitates on substrate topography. Chen et al. [1] reported that a recast layer with a γ phase and κ phase were formed on the Fe–Al–Mn (FAM) alloy surface following electro-discharge machining (EDM). The nano-(γ phase + κ carbide) particles have important roles in the formation of a nanostructured oxide layer that can increase alloy biocompatibility. Moreover, numerous researchers have also demonstrated that Fe–Al–Mn-based alloys were subjected to heat treatment at various temperature ranging; the nano-precipitates were formed in the matrix of the alloys [3,5,7,8]. It is believed that both nanostructural surfaces and nano-precipitates can promote the contact area of the albumin, and then increasing the hemcompatibility and biocompatibility. Hence, for biomedical applications, this study develops and elucidates electro-discharging was employed to treat the FAM alloy surface. The specimens were evaluated by material analysis to determine the properties of treated and untreated

* Corresponding author.
Tel.: +886 2 27361661x5400/5205; fax: +886 2 27395524.
** Co-corresponding author. Tel.: +886 2 22490088x2552.
E-mail addresses: hms4837@yahoo.com.tw (M.-S. Huang), klou@tmu.edu.tw (K.-L. Ou).
[1] Co-first author.

0925-8388/$ – see front matter © 2010 Elsevier B.V. All rights reserved.
doi:10.1016/j.jallcom.2010.06.071

Table 1
Chemical compositions of the investigated alloys.

Alloy	Chemical composition (wt.%)				
	Fe	Al	Mn	C	Cr
A	Bal.	8.82	29.51	–	–
B	Bal.	8.85	30.05	0.58	3.03
C	Bal.	9.10	29.66	0.91	2.87
D	Bal.	8.89	30.03	1.22	3.12
E	Bal.	9.15	30.12	0.62	4.94
F	Bal.	9.01	29.78	0.93	5.15
G	Bal.	8.95	30.63	1.21	4.92
H	Bal.	9.56	30.19	0.64	7.05
I	Bal.	9.13	29.97	0.81	7.10
J	Bal.	8.86	30.16	1.12	6.96

FAM alloys. Furthermore, the biocompatibility of the alloy with and without treatments was also investigated clearly. For easy classification, FAM alloy with EDM treatment, FAM including C and Cr elements without EDM treatment are denoted as FAM-M and FAM-CCr, respectively.

2. Experimental procedures

Ingots of Fe–9Al–30Mn alloy and Fe–9Al–30Mn containing 0.6, 0.9, and 1.2 wt.% C and 3.0, 5.0, and 7.0 wt.% Cr were prepared in an air induction furnace with a protective N_2 atmosphere using AISI 1008 low carbon steel, 99.7% pure electrolytic Al, 99.9% pure electrolytic Mn, pure C powder, and pure Cr. The chemical compositions of the investigated alloys were determined by inductively coupled plasma–atomic emission spectrometry as shown in Table 1. After homogenization at 1200 °C for 4 h in a protective argon atmosphere, the ingots were hot-forged to a final thickness of 3.0 mm. The as-forged specimens were subsequently solution-treated at 1050 °C for 30 min in a vacuum furnace and then quenched rapidly. In addition, some specimens of FAM alloy (i.e. alloy A) were electro-discharge machined using kerosene with a copper electrode and various I_p (pulse electrical current).

The specimens for optical microscopy (OM, Olympus BX-51) were abraded with SiC paper, polished with 1 μm Al_2O_3 powder, washed in distilled water, ultrasonically degreased in acetone, and etched (5–10% nital solution). The phase transformation of the specimens after treatments was examined by transmission electron microscopy (TEM, JEOL JEM-2100). TEM samples were prepared electron transparency by mechanical thinning followed by ion milling in a precision ion polishing system (PIPS, Gatan 691 type).

Cell proliferations on the FAM alloys were investigated in each test, and that on 24-well polystyrene plates was investigated as controls. Alloys under various conditions were placed into the 24-well polystyrene plates, and a MC3T3-E1 cell suspension was placed on the plate with a $5 \times 10^4/cm^2$ density. Plastic culture plates were used as a positive control. After cell culture for 1 h, 8 h, 1 day and 2 days, the cells that did not attach were washed out with PBS (0.1 M, pH 7.2). Into every culture plate, 500 μl culture solution and 50 μl 3-(4,5-dimethylthiazol-2-yl)-2,5-diphenyltetrazolium bromide (MTT) label solution were added, and the plates were put into a culture chamber at 37 °C and under 5% CO_2. Active cells can produce formazan salt for 4 h, after which the buffer solution (10% SDS/0.01 M HCl, 500 μl/well) was added. Overnight, a light of 595 nm wavelength was used to obtain the cell optical density (OD). We repeated the above procedure five times as to obtain the average and compare it with controls. Finally, cell attachment and proliferation were examined by SEM. For immunolabeling of albumin-linked FAM alloys, the alloys were incubated for 10 min with 0.01 M phosphate-buffered saline (PBS, pH 7.2) containing 1% ovalbumin to block nonspecific sticking, and then were incubated for 90 min with a rabbit anti-rat albumin antibody (Cappel) at a dilution of 1 in 250. Specimens were rinsed in PBS and again briefly exposed to PBS-ovalbumin as described above. The sites of antibody–antigen binding were then identified by incubation with the protein A-gold complex for 30 min. The complex was prepared as previously described using 8 nm gold particles. The controls were incubated with a nonimmune antibody followed by that with protein A-gold. The specimens were rinsed with PBS and then distilled water, and then were examined by SEM and AFM. A p-value of 0.05 indicates that the probability of drawing the tested sample is only 5% if the null hypothesis is actually true.

3. Results and discussion

3.1. Microstructural variation of FAM-CCr and FAM-M alloys

Fig. 1(a) displays the optical micrograph of the as-quenched alloy G. It is clearly seen that its microstructure was essentially a single austenite (γ) phase with annealing twins. This microstructural characteristics could also observed in the FAM-CCr alloy with lower C and Cr content (i.e. alloy B through alloy F) after quenched. However, with increasing Cr contents to 7.0 wt.%, it was found that its microstructure became a mixture of γ- and C-precipitates (black region) phases, as illustrated in Fig. 1(b). These C-precipitates were formed in the matrix and on the grain boundaries. Moreover, the amounts of these C-precipitates increased with the C contents. Fig. 2 presents the optical micrograph on the surface recast layer of the alloy A with EDM treatment (FAM-M). Obviously, there is presence of white spot-like phase (M-precipitate) in the recast layer of the treated alloy. The M-precipitate is the phase formed by electro-discharging, revealing that electro-discharging enhances a larger thermal gradient and then induces γ-phase saturates. This is the reason why the FAM-M alloy is associated

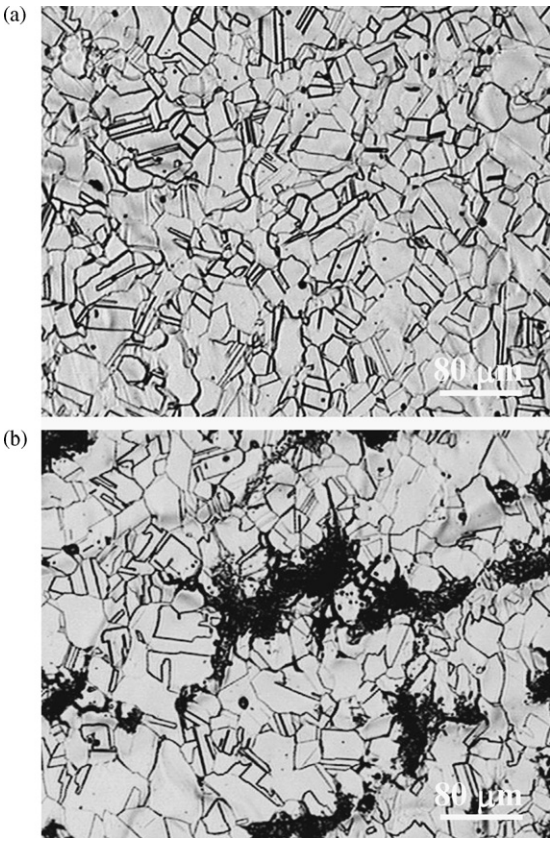

Fig. 1. Optical micrographs of the as-quenched FAM-CCr alloys: (a) alloy G and (b) alloy H.

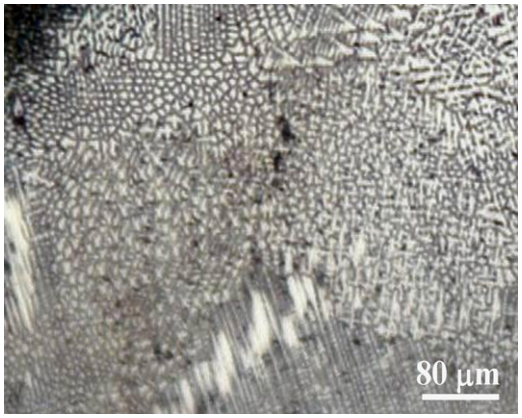

Fig. 2. Optical micrograph of the FAM-M alloy.

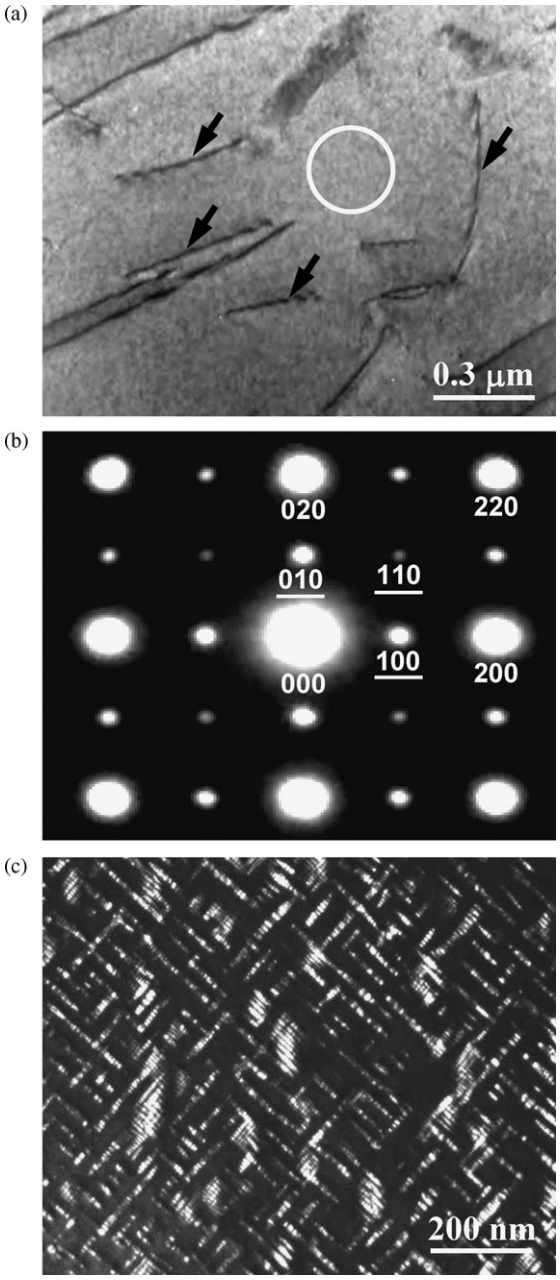

Fig. 3. (a) BF image taken from the γ matrix of the alloy G in Fig. 1(a) and (b) a zone axis [0 0 1] SAEDP taken from the γ matrix, which is marked white circle in (a) (*hkl* = γ phase; *hkl* = κ′-carbide); and (c) $\vec{g} = 100$ κ′-carbide DF.

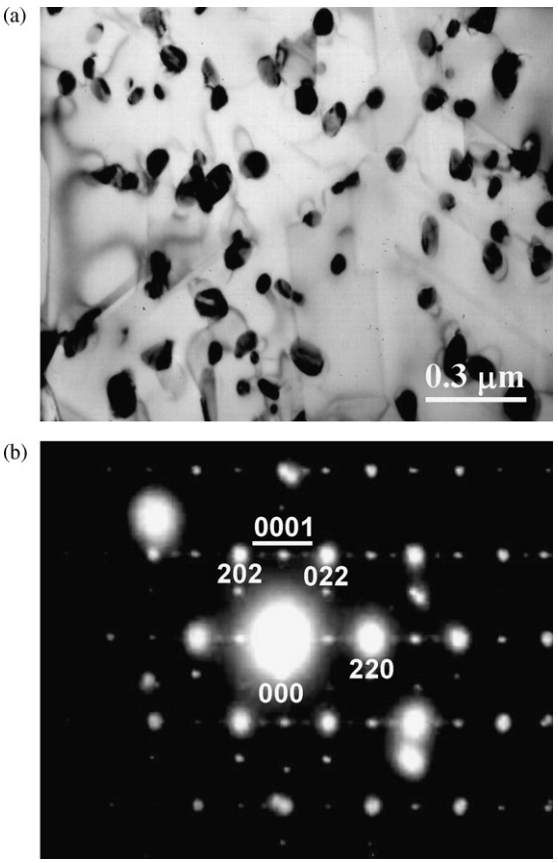

Fig. 4. (a) BF image taken from a mixed region covering the γ- matrix and C-precipitates in Fig. 1(b) and (b) a SAEDP taken along [1 1 1] from the mixed region (*hkl* = γ phase, *hkil* = Cr_7C_3-carbide).

with the formation of saturated precipitate carbide. Moreover, the recast layer has a micro-scale thickness approximately to be 20–50 μm. It was similar to that described by Lim et al. [22]. The thickness of the recast layer is associated with the field-assisted migration of ions in dielectric fluid systems. Solidified layer and molten alloy are formed and rapidly as the field-assisted migration of ions proceeds continuously. Hence, the crystalline microstructure of the recast layer consists of a γ- and M-precipitate phases.

Fig. 3(a) shows a bright field (BF) electron micrograph taken from the γ matrix of the alloy G in Fig. 1(a), revealing the presence of dislocations (as indicated by arrows) within the γ matrix. Fig. 3(b) depicts a zone axis [0 0 1] selected area electron diffraction pattern SAEDP taken from the γ matrix, which is marked white circle in Fig. 3(a), indicating that the γ matrix has a face-centered-cubic structure with lattice parameter $a = 0.380$ nm. Moreover, it is clearly seen that in addition to the reflection spots of the γ phase, the SAEDP also comprises small superlattice spots. Chao and Liu [23] demonstrated that the intensity of the (1 0 0) spot for the $L'1_2$ structure is much stronger than that of the (1 1 0) spot. Further, the intensities of the (1 0 0) and (1 1 0) spots of the $L1_2$ structure are similar. Therefore, it was concluded that these superlattice spots correspond to κ′-carbides ($(Fe,Mn)_3AlC_x$) having an ordered $L'1_2$ structure with lattice constant $a = 0.368$ nm [3,5,23] and that fine κ′-carbides were formed in the matrix by spinodal decomposition during quenching [3,5]. Fig. 3(c) shows a $\vec{g} = 100$ κ′-carbide dark field (DF) electron micrograph that clearly reveals the formation of the fine κ′-carbide in the γ matrix. Accordingly, the microstructures of the FAM-CCr alloy with lower C and Cr content (i.e. alloy B through alloy G) following solution-treated at 1050 °C was the γ phase containing fine κ′-carbides.

Fig. 4(a) displays a BF electron micrograph taken from a mixed region covering the γ-matrix and C-precipitates in Fig. 1(b). The figure indicates that some particle precipitates formed in the γ matrix and at the twin boundaries. Fig. 4(b) shows a SAEDP taken along [1 1 1] from the mixed region, revealing small satellites spots in addition to the reflection spots of the γ phase. From the camera length and *d*-spacings of the satellites spots, suggesting that the C-precipitates are Cr_7C_3 carbides (Cr-carbide) with a hexagonal structure and lattice parameters $a = 1.393$ nm and $c = 0.455$ nm [3,8]. Therefore, the microstructure of the FAM-CCr alloy with higher Cr contents (i.e. alloy H through alloy J) was a mixture of the γ and Cr_7C_3 phases.

Fig. 5 displays TEM micrographs of FAM and FAM-M alloys. Fig. 5(a) shows a BF electron micrograph of FAM alloy, which was

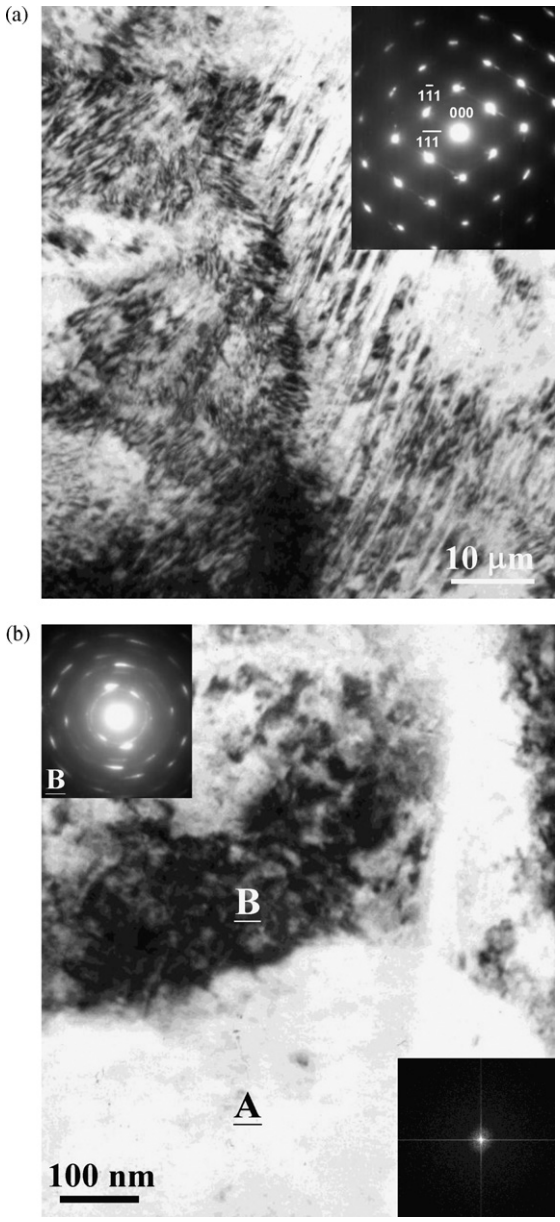

Fig. 5. TEM micrographs of FAM and FAM-M alloys: (a) BF image of FAM alloy (zone = [0 0 1]) and (b) BF image and SAEDP of FAM-M alloy.

taken from the γ matrix under two-beam condition in the [0 0 1] zone, revealing the presence of the modulated structure within the matrix. Only γ matrix with numerous annealing twins could be examined. Fig. 5(b) presents a BF image and SAEDP of FAM-M alloy. The figures demonstrate the presence of various microstructures in the alloy matrix. Fig. 5(b) also depicts an SAEDP of an area denoted as A. No diffraction spot is obtained from area A, indicating that the amorphous glass metal was formed on the recast layer. The diffraction ring pattern is an electron diffraction pattern, instead of a pattern of nondiffraction spots, from the area (B), revealing that the B-area is a nanostructure. From the camera length and *d*-spacings of the reflection spots, the crystal structure of the M-precipitate was determined to be $Fe_{0.6}Mn_{5.4}C_2$ (κ-carbide) having a hexagonal structure with lattice parameter $a = 5.77$ nm and $c = 6.98$ nm [1]. Therefore, the microstructure of an electro-discharged alloy was a mixture of nano-(γ-phase + κ-carbide). The grain size of the carbides was only 20 nm, indicating that not only was the nanophase formed during electro-discharging reactions, but also electro-bombardment was responsible for nanocrystallization.

As stated above, the crystalline structure of FAM-M consists of γ-phase and κ-carbide, revealing that carbon saturates the γ-phase and that a larger thermal gradient is associated with the formation of saturated carbide. The above investigation demonstrates that the recast layer was formed by FAM-M alloy following high electro-discharging energy. The electro-discharging energy may dissolve and impact more carbon and/or carbon species from the dielectric fluid as the electro-discharging energy increases, and cause the formation of super-saturated γ-phase and more carbide on the rapid cooling FAM-M alloy surface. During electro-discharging treatment, a chemical reaction of the equivalent activation energy is conducted to overcome the surface activation energy. This equivalent activation energy from the etchant. In the electro-discharging reaction, the etchant activation energy is the redox potential in the etching reaction of alloy in electrolyte. The surface activation energy acts as a barrier. As the etchant activation energy exceeds the surface activation energy, the reaction can be preceded. The alloy surface without electro-discharging initially has higher surface activation energy than the alloy surface with electro-discharging. The formation of κ-carbide and phase transformation from γ-phase to κ-carbide is associated with the thermal gradient during electro-discharging. It is believed that surface activation energy can be effectively decreased as formation rate of κ-carbide. Additionally, the formation of nanostructural κ-carbide increases the grain boundaries and sub-grain boundaries on the alloy matrix, reducing the surface activation energy. Furthermore, during electro-discharging, nucleation and growth solidified liquid metals, and over cooling can stabilize nucleation and control the nucleation rate. Liquid metals are easily nucleated, preventing them from becoming metal glass, because they are more viscous and crystallize fast. An amorphous metal must typically have a high cooling rate [24]. Phase transformation during supercooling is responsible for the complex microstructures in the recast layer.

3.2. Biocompatibility of FAM, FAM-CCr and FAM-M alloys

Fig. 6 shows the morphology of cross-linked albumin on FAM, FAM-CCr and FAM-M alloys, and reveals circular spots and clusters. The figure reveals that the FAM, FAM-CCr and FAM-M alloys had a thin cross-linking layer. Albumin was detected by immunogold labeling, where the distribution and density of the labeling were visualized by atomic force microscopy. Both freshly prepared FAM, FAM-CCr and FAM-M alloys and similar samples stored in buffer for 1 week provided comparable results and demonstrated a generally uniform labeling of the FAM, FAM-CCr and FAM-M alloys, although some areas of the FAM, FAM-CCr and FAM-M alloys illustrated a lower density of gold particles. These data demonstrate that the albumin is stably bound and retains its antigenicity after various steps of the linking procedure. Furthermore, the density of labeling obtained suggests that the albumin linkage is efficient. Fig. 6(a) illustrates a FAM alloy after labeling. The control sample was incubated only with protein A-gold and displays a background labeling of fewer gold particles. Fig. 6(b) shows a representative area of the FAM-CCr and FAM-M alloys after labeling. It was found that the nano-gold labeling density of the FAM-CCr and FAM-M alloys are 457 and 569 particles/μm^2, respectively, which is below the experimental value, reflecting the expected nonspecific adsorption of albumin. The albumin adsorbed onto the surface increased with increasing nano-carbides following surface treatment. It illustrated that the adsorption amount of albumin increased with increasing the surface oxide thickness with nanocrystallization. Based on the investigation, the oxidation by electro-discharging enhances the biocompatibility of the implant surfaces. As stated above, surface nano-precipitates and functionalized modification by surface

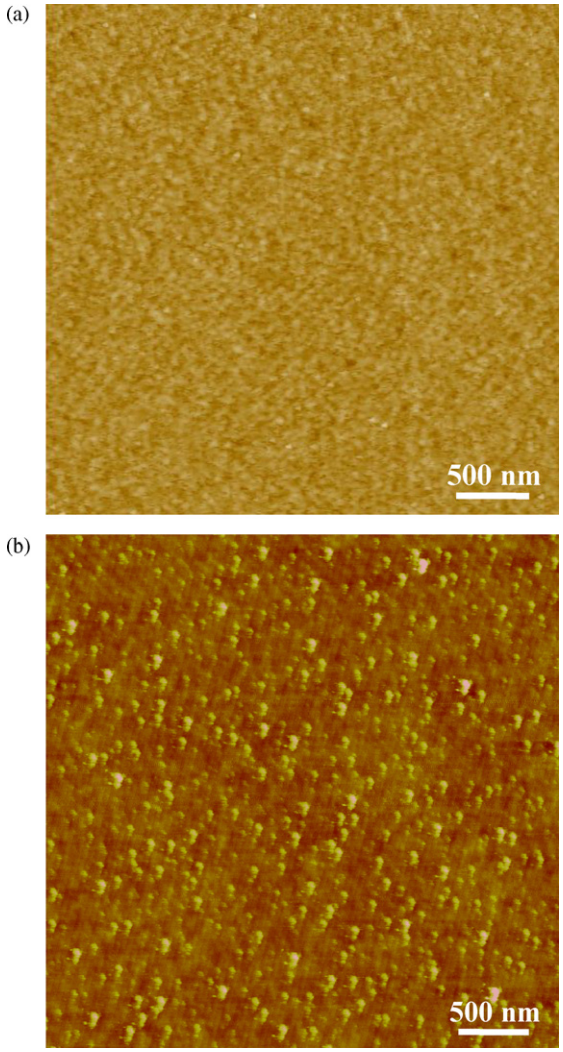

Fig. 6. The morphology of cross-linked albumin on FAM, FAM-CCr and FAM-M alloys: (a) FAM alloy and (b) FAM-CCr and FAM-M alloys.

treatments are believed to improve tissue healing. Albumin-grafted contact systems with high biocompatibility can also be obtained. A porous structure is typically obtained by immersion and/or dipping in alkaline solution [18]. A three-dimensional nanoporous network structure and a thicker titanium oxide layer were observed following anodization and cathodic pretreatments [25,26]. Nanoporous structures and the volcano-like and re-solidified molten metals were observed on the EDM-treated surface [1,10]. As is widely believed, the thicker oxide layer and porosity are responsible for the improved implant performance. It is believed that the biocompatible improvement of implants is attributable to the thicker oxide layer and porosity, which enhances the adhesion between artificial bone and genuine bone [18,19]. In the researches of bone tissue engineering, a three-dimensional porous scaffold and structure is helpful for cell attachment, proliferation and differentiation [27]. Furthermore, bone plate with nanostructral titania film can effectively decrease surface stiffness of the plate (the stiffness ratio of nanostructral titania and titanium is approach 1:3.5), and diminished stress shielding [28]. A number of reports have described the occurrence of bone loss around implants in animals [29]. The studies indicated that some bone loss occurred for both the machined implants and partially porous implants while no significant bone loss were seen with fully porous implants. For porous implants, bone loss can be avoided by extending the porous coverage of the implant coronally. In addition, the low stiffness of implant surfaces can enhance the compactable stress distribution around the implants, thereby avoiding the abnormal high stress causing microfracture and subsequent resorption of the bone contacting the implant. Fig. 7 schematically depicts mechanisms of formation oxide layer on the FAM alloys with and without treatment. Oxygen was absorbed on the surface in the environment, and FAM alloys undergo oxygen absorption reaction (as shown in upper Fig. 7(a) and (b). The depth of oxygen was limited to close to the surface and the amount of oxygen was extremely low; this oxygen penetrated into the specimen during chemical etching in a mixed acid solution [1,10], revealing that the amounts of oxygen were so low that a oxide layer could not be formed. Hence, a porous structure was not observed on the surface, and native oxide was thin, as displayed in lower Fig. 7(a). The oxide films against the diffusion of metal ions can be improved by increasing the thickness of the oxide. Furthermore, increasing the thickness of the oxide layer on alloys clearly enhances the biocompatibility [25,26]. The oxide layer formed by heat treatment has a ~200 nm thick and a microporous structure, as shown in lower Fig. 7(b), indicating that the oxide layer with κ′-carbide and Cr-carbide was prepared by heat treatment. In addition, the oxygen absorption reaction and formation of ion bombardment play a critical factor in forming a porous oxide film during electro-discharging. As presented in upper Fig. 7(c), the absorption and charging of oxygen may induce a phase transformation

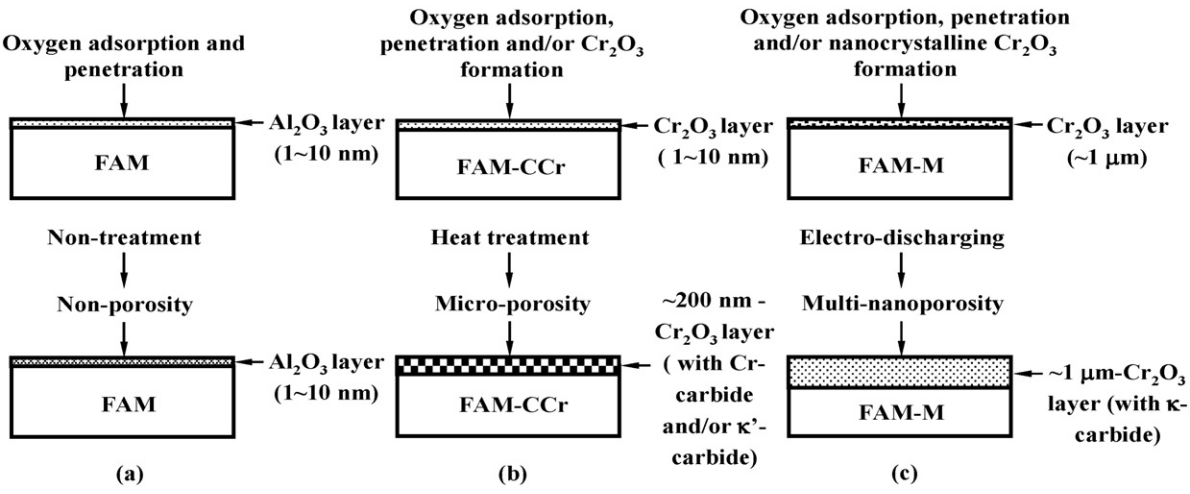

Fig. 7. Mechanisms of formation oxide layer on the FAM alloys with and without treatment: (a) FAM alloy; (b) FAM-CCr alloys; and (c) FAM-M alloy.

from γ-phase to nano-(γ-phase + κ-carbide). As nano-κ-carbide is present on the surface during initial ion bombardment, the nano-κ-carbide phases are dissolved by electro-discharging, making the multi-nanoporous surface, as shown in lower Fig. 7(c). The absorption of oxygen or the formation of nano-κ-carbide phase is essential to generating the nanoporous oxide layer by electro-discharging. Electro-discharging changes the enthalpy of the system, because the thickness of the oxide film can typically be limited [1,10]. The redox reaction dominates the formation of an oxide layer. The penetration and reaction of oxygen result in the formation of nano-metal carbides on the surface. The surface that contains nanophases is readily dissolved in the alkaline solution, and nanoporous oxide is formed by chemical treatment for a short period at room temperature. The formation of nano-metal carbides and the dissolution of nano-metal carbides are thought to be critical in the formation of a nanoporous oxide film. As stated above, determining whether the oxygen can reach the surface is important. At room temperature, a native oxide layer serves as a barrier to the diffusion of oxygen and blocks the desorption of oxygen. During electro-discharging, over the range of temperatures at which desorption occurs; the native oxide that covers the surface begins to decompose [30]. The temperature during oxygen charging first increases the rate of diffusion of oxygen and then reduces the thickness of the diffusion barrier formed from the native oxide. The decomposition and dissolution of the nano-metal carbides would represent an alternative mechanism of the activation of desorption during electro-discharging and then the thick and multi-nanoporous oxide can be obtained.

4. Conclusions

As quenched, the microstructure of the FAM-CCr alloy with lower C and Cr content was the γ phase containing fine κ′-carbides. The microstructure of the FAM-CCr alloy with higher Cr contents was a mixture of the γ and Cr_7C_3 phases. Furthermore, for FAM-M alloy with surface treatment. The recasting layer was formed on FAM-M, and it consists of a γ-phase and κ-carbide. The κ-carbide has a hexagonal structure with lattice parameter $a = 5.77$ nm and $c = 6.98$ nm. Therefore, the microstructure of FAM-M alloy was a mixture of nano-(γ-phase + κ-carbide). The grain size of the κ-carbides was only 20 nm, indicating that not only was the nanophase formed during electro-discharging reactions, but also electro-bombardment was responsible for nanocrystallization. The formation of metal-carbides can enhance anti-wearing capability, then improving metal ion releasing under body surroundings. Thus, it is believed that the FAM-based alloys containing metal-carbides can enhance biocompatibility.

Acknowledgements

The authors would like to thank the Center of Excellence for Clinical Trial and Research in Neurology and Neurosurgery, Taipei Medical University-Wan Fang Hospital for financially supporting this research under contract No. DOH99-TD-B-111-003 and supported partly by Department of Health, Executive Yuan, Taiwan under contract No. DOH99-TD-N-111-04. The authors would also like to thank Biomate Medical Devices Technology Co., Ltd. for financially supporting this research under contract No. EZ-04-06-10-98.

References

[1] S.L. Chen, M.H. Lin, C.C. Chen, K.L. Ou, J. Alloys Compd. 456 (2008) 413.
[2] S. Kumar, T.S.N. Sankara Narayanan, J. Alloys Compd. 479 (2009) 699.
[3] C.F. Huang, K.L. Ou, C.S. Chen, C.H. Wang, J. Alloys Compd. 488 (2009) 246.
[4] T.C. Niemeyer, C.R. Grandini, L.M.C. Pinto, A.C.D. Angelo, S.G. Schneider, J. Alloys Compd. 476 (2009) 172.
[5] C.S. Chen, C.T. Lin, P.W. Peng, M.S. Huang, K.L. Ou, L.H. Lin, C.H. Yu, J. Alloys Compd. 493 (2010) 346.
[6] J.H. Han, D.H. Park, C.W. Bang, S. Yi, W.H. Lee, K.B. Kim, J. Alloys Compd. 483 (2009) 44.
[7] M.S. Chen, H.C. Cheng, C.F. Huang, C.Y. Chao, K.L. Ou, C.H. Yu, Mater. Charact. 61 (2010) 206.
[8] C.M. Liu, H.C. Cheng, C.Y. Chao, K.L. Ou, J. Alloys Compd. 488 (2009) 52.
[9] M.C. Chang, C.W. Luo, M.S. Huang, K.L. Ou, L.H. Lin, H.C. Cheng, J. Alloys Compd. 499 (2010) 171.
[10] P.W. Peng, K.L. Ou, H.C. Lin, Y.N. Pan, C.H. Wang, J. Alloys Compd. 492 (2010) 625.
[11] Josefina Ballarre, Inderchand Manjubala, H. Wido, Schreiner, Juan Carlos Orellano, Peter Fratzl, Silvia Ceré, Acta Biomater. 6 (4) (2010) 1601.
[12] M. Roach, Dent. Clin. N. Am. 51 (2007) 603.
[13] S. Nagarajan, N. Rajendran, Appl. Surf. Sci. 255 (2009) 3927.
[14] M.H. Ding, B.L. Wang, L. Li, Y.F. Zheng, Surf. Coat. Technol. 204 (2010) 2519.
[15] H.C. Cheng, S.Y. Chiou, C.M. Liu, M.H. Lin, C.C. Chen, K.L. Ou, J. Alloys Compd. 477 (2009) 931.
[16] Z. Yang, J. Wang, R. Luo, M.F. Maitz, F. Jing, H. Sun, N. Huang, Biomaterials 31 (8) (2010) 2072.
[17] R.J. Keogh, J.W. Eaton, J. Lab. Clin. Med. 124 (1994) 537.
[18] K.L. Ou, J. Wu, W.F. Lai, C.B. Yang, W.C. Lo, L.H. Chiu, J. Bowley, J. Biomed. Mater. Res. A 92 (3) (2010) 906.
[19] W.C. Feng, C.H. Wang, H.C. Cheng, S.Y. Chiou, C.S. Chen, K.L. Ou, J. Vac. Sci. Technol. B 27 (2009) 1559.
[20] K.L. Ou, C.T. Lin, S.L. Chen, C.F. Huang, H.C. Chen, Y.M. Yeh, K.H. Ling, J. Electrochem. Soc. 155 (2008) 79.
[21] W.J. Chang, K.L. Ou, S.Y. Lee, J.Y. Chen, Y. Abiko, C.T. Lin, H.M. Huang, Dent. Mater. J. 27 (3) (2008) 340.
[22] L.C. Lim, L.C. Lee, Y.S. Wong, H.H. Lu, Mater. Sci. Technol. 7 (1991) 239.
[23] C.Y. Chao, C.H. Liu, Mater. Trans. 43 (2002) 2635–2642.
[24] P. Duwez, ASM Trans. 60 (1967) 607.
[25] Y.C. Shyng, H. Devlin, K.L. Ou, Int. J. Prosthet. 19 (5) (2006) 513.
[26] H.C. Cheng, S.Y. Lee, C.C. Chen, Y.C. Shyng, K.L. Ou, Appl. Phys. Lett. 89 (2006) 173902.
[27] S.S. Liao, F.Z. Cui, Y. Zhu, J. Bioact. Compos. Poly 19 (2004) 117.
[28] C.C. Lin, H.C. Cheng, C.F. Huang, C.T. Lin, S.Y. Lee, C.S. Chen, K.L. Ou, J. Appl. Phys. 44 (12) (2005) 8590.
[29] R.B. Heimann, N. Schurmann, R.T. Muller, J. Mater. Sci. 15 (2004) 1045.
[30] M. Jobin, M. Taborelli, P. Descouts, Appl. Surf. Sci. 72 (1993) 363.